PHYSICAL REVIEW B VOLUME 52, NUMBER 4 15 JULY 1995-II

Generation of optical standing waves around mesoscopic surface structures: Scattering and light confinement

Christian Girard
Laboratoire de Physique Moléculaire UA CNRS 772, Université de Franche-Comté, 25030 Besançon cedex, France

Alain Dereux
Institute for Studies in Interface Sciences, Facultés Universitaires Notre-Dame de la Paix, Rue de Bruxelles 61, B-5000 Namur, Belgium

Olivier J. F. Martin
Swiss Federal Institute of Technology, ETH-Zentrum CH-8092 Zurich, Switzerland

Michel Devel
Laboratoire de Physique Moléculaire UA CNRS 772, Université de Franche-Comté, 25030 Besançon cedex, France

(Received 16 December 1994; revised manuscript received 3 March 1995)

Optical scanning probe devices offer an extremely efficient way of collecting local information on the complex structure of optical electromagnetic fields lying near a surface. This paper discusses recent theoretical efforts to develop an efficient method for the calculation of the field distributions in experimentally relevant near-field and integrated optics systems. In order to overcome the obstacles inherent in the matching of the electromagnetic boundary conditions on the surface of complex objects, the discussion is presented in the framework of the integral-equation formalism. This treatment is based on the field-susceptibility Green-function technique applied in real space. Two original numerical schemes, both based on a different discretization procedure, are discussed, and several numerical applications on systems of experimental interest are presented. Particularly, the problem of near-field distribution around three-dimensional objects of various sizes and shapes is investigated as a function of experimental parameters.

I. INTRODUCTION

Scanning probe devices offer an extremely efficient way of collecting local information on the complex structure of optical electromagnetic fields lying near a surface of arbitrary profile.[1-18] Over the past few years, numerous optical experiments based on concepts borrowed from the scanning tunneling microscope (STM) have appeared. Henceforth, these experiments have clearly demonstrated the possibility to increase the optical resolution far beyond the Rayleigh limit.

Usually, in scanning near-field optical microscopy (SNOM) emphasis is generally directed toward the extraordinary lateral resolution that can be reached. In addition, this local probe technique offers numerous other interesting features, e.g., the possibility to map the structure of the electromagnetic field inside a Fabry-Pérot resonator,[19] to image localized plasmons over a metallic surface,[20] and to detect evanescent fields in guiding structures.[21] These last applications were developed with the scanning tunneling optical microscope (STOM) configuration in which the sample is illuminated in total internal reflection.[9,10,13-16] By analogy with the tunnel effect of electrons used in STM, this experimental configuration is also named the photon scanning tunneling microscope (PSTM).

In this paper we discuss solutions of Maxwell's equations for both the mesoscopic and nanometric regimes, which are at the center of the present drive towards the ongoing optical experimentations at the nanometer scale. Recently,[22] we developed a theoretical approach to study the main features of the physical interaction between a thin probe tip and a corrugated surface. This study was based on a self-consistent calculation of the optical coupling between tip and sample.[22] In the present work, we apply the same framework to derive the whole field distribution around three-dimensional (3D) mesoscopic objects of arbitrary shape deposited on a flat surface under STOM illumination. More specifically, this work will study how optical near-field variations result from the interaction of an extended light beam or a surface wave with mesoscopic objects: a phenomenon that we will define as confinement since the near fields built up near the nanometer size structures are strongly confined and enhanced compared to the average field distribution. For this purpose, we will introduce in Sec. II the field-susceptibility Green's-function technique, which allows us to obtain general solutions of Maxwell's equations by means of a Lippmann-Schwinger integral equation.[23-27] Associated with an appropriate discretization procedure in real space, such an integral representation avoids the traditional boundary condition problem and therefore can deal with localized objects of arbitrary shape and dielectric constant. From this flexible framework, we will

0163-1829/95/52(4)/2889(10)/$06.00

address in Sec. III the fundamental problem concerning the relation between the field pattern, resulting from the interaction with an incoming surface wave with a 3D object, and the profile of the object itself. In fact, the study of the gradual transition between far-field and near-field regimes is also of interest for experimentalists working in SNOM since it might allow one to determine the precise fundamental difference between pure topographic signals and artifacts originating from interference and scattering phenomena. For example, the recent STOM/PSTM observations of standing field patterns occurring around subwavelength-sized latex spheres deposited on a flat surface, clearly indicate that the amplitude of both fringes patterns and field confinements is very sensitive to the size of the scattering particles. For larger objects the interference generally dominates and makes difficult the detection of subwavelength features.[28] In order to get more insight about this important question, we will present in Sec. III a detailed numerical study about the evolution of the standing field pattern as a function of the dimensions of the object.

II. A REAL-SPACE APPROACH FOR COMPLEX OPTICAL SYSTEMS

As described in the previous section, traditionally Maxwell's equations are solved by matching boundary conditions. Nevertheless, for both arbitrary shapes and optical constants, general solutions of Maxwell's equations can also be obtained with the integral-equation formalism. This section will be devoted to the application of such a real-space approach to the computation of the field distributions lying around three-dimensional objects deposited on a surface, as a function of the usual experimental parameters (object sizes, incident polarization, light beam direction, etc.).

A. The integral-equation formalism

In this subsection, we present a brief description of the concept of retarded field susceptibility in the presence of a 3D system of arbitrary shape and size. Starting from the microscopic Maxwell equations expressed in terms of both charge and current densities, we express the response of a localized physical system submitted to an external electromagnetic excitation (cf. Fig. 1).

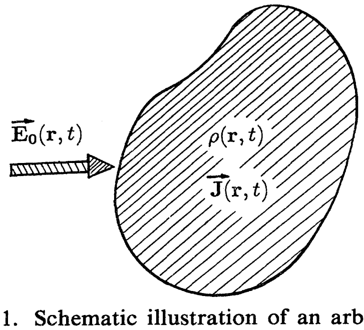

FIG. 1. Schematic illustration of an arbitrary material system submitted to an external electromagnetic field $\mathbf{E}_0(\mathbf{r},t)$. $\rho(\mathbf{r},t)$ and $\mathbf{J}(\mathbf{r},t)$ represent the charge and the current densities induced inside the material.

Let us consider a nonmagnetic physical system characterized by its charge density $\rho(\mathbf{r},t)$ and its current density $\mathbf{j}(\mathbf{r},t)$. Maxwell's equations being linear equations, the response of a given system to an arbitrary wave packet can be obtained from the superpositions of the responses of this system to the individual plane waves forming the original wave packet. We can therefore assume a monochromatic field with a time dependence of the form $e^{-i\omega t}$. With these assumptions, Maxwell's equations in cgs system read

$$\nabla\times\mathbf{E}(\mathbf{r},\omega)=\frac{i\omega}{c}\mathbf{B}(\mathbf{r},\omega)\ , \tag{1}$$

$$\nabla\cdot\mathbf{B}(\mathbf{r},\omega)=0\ , \tag{2}$$

$$\nabla\cdot\mathbf{E}(\mathbf{r},\omega)=4\pi\rho(\mathbf{r},\omega)\ , \tag{3}$$

and

$$\nabla\times\mathbf{B}(\mathbf{r},\omega)=-\frac{i\omega}{c}\mathbf{E}(\mathbf{r},\omega)+\frac{4\pi}{c}\mathbf{j}(\mathbf{r},\omega)\ . \tag{4}$$

The vectorial wave equation for the electric field is readily obtained by taking the curl of Eq. (1). After some straightforward algebra, one gets the well-known result

$$\Delta\mathbf{E}(\mathbf{r},\omega)+k_0^2\mathbf{E}(\mathbf{r},\omega)=4\pi\nabla\rho(\mathbf{r},\omega)-ik_0\frac{4\pi}{c}\mathbf{j}(\mathbf{r},\omega)\ , \tag{5}$$

where $k_0=\omega/c$ represents the wave vector associated to the frequency ω.

We express now both charge and current densities in terms of the local polarization $\mathbf{P}(\mathbf{r},\omega)$ of the material system:

$$\rho(\mathbf{r},\omega)=-\nabla\cdot\mathbf{P}(\mathbf{r},\omega)\ , \tag{6}$$

and

$$\mathbf{j}(\mathbf{r},\omega)=-i\omega\mathbf{P}(\mathbf{r},\omega)\ . \tag{7}$$

We now rewrite the nonhomogeneous equation (5) as

$$\Delta\mathbf{E}(\mathbf{r},\omega)+k_0^2\mathbf{E}(\mathbf{r},\omega) =-4\pi\{\nabla[\nabla\cdot\mathbf{P}(\mathbf{r},\omega)]+k_0^2\mathbf{P}(\mathbf{r},\omega)\}\ . \tag{8}$$

Let $\mathbf{E}_0(\mathbf{r},\omega)$ be the solution of the following homogeneous equation:

$$\Delta\mathbf{E}_0(\mathbf{r},\omega)+k_0^2\mathbf{E}_0(\mathbf{r},\omega)=0\ . \tag{9}$$

The general solution of (8) is the sum of the homogeneous field $\mathbf{E}_0(\mathbf{r},\omega)$ plus a particular solution $\mathbf{E}_m(\mathbf{r},\omega)$. This particular solution can be derived from the knowledge of the scalar free-space Green's function[29,30]

$$\mathcal{G}_0(\mathbf{r},\mathbf{r}',\omega)=\frac{e^{ik_0|\mathbf{r}-\mathbf{r}'|}}{|\mathbf{r}-\mathbf{r}'|}\ , \tag{10}$$

with

$$\Delta\mathcal{G}_0(\mathbf{r},\mathbf{r}',\omega)+k_0^2\mathcal{G}_0(\mathbf{r},\mathbf{r}',\omega)=-4\pi\delta(\mathbf{r}-\mathbf{r}')\ . \tag{11}$$

By applying the standard Green's-function technique, one finds

$$\mathbf{E}_m(\mathbf{r},\omega)=\int \mathbf{S}_0(\mathbf{r},\mathbf{r}',\omega)\cdot\mathbf{P}(\mathbf{r}',\omega)d\mathbf{r}' \ , \tag{12}$$

where $\mathbf{S}_0(\mathbf{r},\mathbf{r}',\omega)$ defines the free-space dyadic propagator[29-33] (also called dyadic field susceptibility)

$$\mathbf{S}_0(\mathbf{r},\mathbf{r}',\omega)=(k_0^2+\nabla\nabla)\mathcal{G}_0(\mathbf{r},\mathbf{r}',\omega) \ . \tag{13}$$

At this stage the Lippmann-Schwinger equation can be deduced from the previous results. First, we write the complete solution of (8) as the sum of both homogeneous and inhomogeneous solutions:

$$\mathbf{E}(\mathbf{r},\omega)=\mathbf{E}_0(\mathbf{r},\omega)+\mathbf{E}_m(\mathbf{r},\omega) \ . \tag{14}$$

Second, we introduce the usual constitutive equation for a local medium,

$$\mathbf{P}(\mathbf{r},\omega)=\chi(\mathbf{r},\omega)\cdot\mathbf{E}(\mathbf{r},\omega) \ . \tag{15}$$

Finally, by substituting Eq. (15) into Eq. (12) and the resulting formula into Eq. (14), we find

$$\mathbf{E}(\mathbf{r},\omega)=\mathbf{E}_0(\mathbf{r},\omega) + \int \mathbf{S}_0(\mathbf{r},\mathbf{r}',\omega)\cdot\chi(\mathbf{r}',\omega)\cdot\mathbf{E}(\mathbf{r}',\omega) \ . \tag{16}$$

This last equation is very general. Indeed, if we introduce an additional perturbation due to, for example, the presence of an extended medium (the surface of a semi-infinite material, a macroscopic sized particle, etc.), we only need to replace the free-space dyadic $\mathbf{S}_0(\mathbf{r},\mathbf{r}',\omega)$ by

$$\mathbf{S}(\mathbf{r},\mathbf{r}',\omega)=\mathbf{S}_0(\mathbf{r},\mathbf{r}',\omega)+\mathbf{S}_s(\mathbf{r},\mathbf{r}',\omega) \ , \tag{17}$$

where the additional contribution $\mathbf{S}_s(\mathbf{r},\mathbf{r}',\omega)$ accounts for the dynamical response of such an extended system.

Before discussing various efficient numerical procedures to solve Eq. (16), we would like to give more details about the physical meaning of such response functions. The field susceptibility $\mathbf{S}_s(\mathbf{r},\mathbf{r}',\omega)$ of a material system reveals how a dipolar source field is modified at the proximity of the surface limiting this system.[29-34] In a general quantum description, this response function can be expressed in terms of the matrix elements of the field operator associated with the material system.[29] The deduction of the response field of the solid to a fluctuating dipole moment is another way of deriving this susceptibility. In the particular case of a solid limited by a perfectly planar surface, various theoretical methods have been developed to derive this dyadic tensor (cf. Appendix). The analytical form of $\mathbf{S}_s(\mathbf{r},\mathbf{r}',\omega)$ depends on the nature of the surface investigated. To treat a crystallographic face of an ionic crystal, a discrete atomic representation of the solid structure must be adopted. For a metallic surface displaying mesoscopic roughness, this susceptibility can be modeled from a continuous description of the matter.

In surface physics the use of the field susceptibility concept has proved to be a very fruitful way to understand various physical mechanisms occurring in physisorption experiments. For example, in the case of solid-gas interactions, MacLachlan demonstrated that the field susceptibility associated with the substrate is the fundamental quantity for describing the dispersion energy between adsorbed species and solids. The trace of this dyadic tensor $\mathbf{S}_s(\mathbf{r},\mathbf{r}',\omega)$ when contracted with the dynamical polarizability $\alpha_a(\omega)$ of the adsorbate gives the first-order dispersion energy after integration over imaginary frequencies ($\omega=iu$).[29] In the numerical work to be discussed in this paper, the analytical form for $\mathbf{S}_s(\mathbf{r},\mathbf{r}',\omega)$ can be found in the Appendix.

B. Real-space discretization procedures

The purpose of this section is to describe two different numerical methods for solving Eq. (16) for arbitrary optical systems. For simplicity, we restrict our attention to local, homogeneous, and isotropic materials so that we can express the response function $\chi(\mathbf{r},\omega)$ in terms of the local dielectric constant $\epsilon(\omega)$:

$$\chi(\mathbf{r},\omega)=\frac{\epsilon(\omega)-1}{4\pi} \tag{18}$$

for all points $\mathbf{r}$ located inside the material system, and

$$\chi(\mathbf{r}',\omega)=0 \tag{19}$$

elsewhere (cf. Fig. 2).

(i) Direct resolution of Lippmann-Schwinger equation —The three-dimensional discretization of the Lippmann-Schwinger equation in real space leads to[26,27]

$$\mathbf{E}(\mathbf{r},\omega)=\mathbf{E}_0(\mathbf{r},\omega) + \frac{\epsilon(\omega)-1}{4\pi}\sum_{i=1}^{n} W_i\mathbf{S}(\mathbf{r},\mathbf{R}_i,\omega)\cdot\mathbf{E}(\mathbf{R}_i,\omega) \ , \tag{20}$$

where W_i represents the volume of the ith discretized element and n is the total number of volume element (cf. Fig. 2). The set of unknown vectors $\{\mathbf{E}(\mathbf{R}_i,\omega)\}$ can be determined by standard linear algebra procedure. Thus by setting $\mathbf{r}=\mathbf{R}_k$ in Eq. (20), one obtains the following matrix equation to be solved numerically:

$$\mathcal{A}(\omega)\bullet\mathcal{F}(\omega)=\mathcal{F}_0(\omega) \ , \tag{21}$$

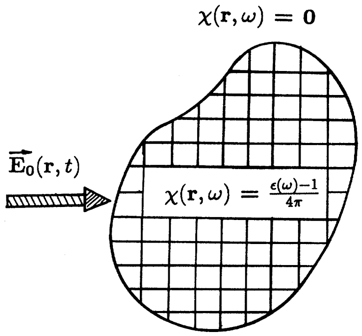

FIG. 2. Schematic diagram of a grid formed by n elementary cells of volume W_i; $i=1,\ldots,n$. When it is extended to the entire volume occupied by the system, this grid can be used to solve the self-consistent scattering problem. In the framework of a local response approach, the dielectric properties of the discretized cells of the grid are related to the optical dielectric constant of the material.

where the symbol ● indicates a total contraction on both Cartesian indices and positions of discretized elements. Moreover, $\mathcal{F}(\omega)$ and $\mathcal{F}_0(\omega)$ are two supervectors defined by

$$\mathcal{F}(\omega)=\{\mathbf{E}(\mathbf{R}_1,\omega);\mathbf{E}(\mathbf{R}_2,\omega);\ldots;\mathbf{E}(\mathbf{R}_n,\omega)\}\ , \tag{22}$$

and

$$\mathcal{F}_0(\omega)=\{\mathbf{E}_0(\mathbf{R}_1,\omega);\mathbf{E}_0(\mathbf{R}_2,\omega);\ldots;\mathbf{E}_0(\mathbf{R}_n,\omega)\}\ . \tag{23}$$

In Eq. (21), the $(3n\times 3n)$ matrix $\mathcal{A}$ is built from different components taken by the field susceptibility $\mathbf{S}$ for all possible couples of position vectors $\{\mathbf{R}_i,\mathbf{R}_k\}$

$$\mathcal{A}(\omega)=\left[\mathbf{I}-\frac{\epsilon(\omega)-1}{4\pi}\mathcal{B}(\omega)\right]\ , \tag{24}$$

where $\mathbf{I}$ represents the identity tensor, and $\mathcal{B}(\omega)$ is the $(3n\times 3n)$ matrix defined by

$$\mathcal{B}(\omega)=\begin{bmatrix} W_1\mathbf{S}(\mathbf{R}_1,\mathbf{R}_1,\omega) & W_2\mathbf{S}(\mathbf{R}_1,\mathbf{R}_2,\omega) & \cdots & W_n\mathbf{S}(\mathbf{R}_1,\mathbf{R}_n,\omega)\\ W_1\mathbf{S}(\mathbf{R}_2,\mathbf{R}_1,\omega) & W_2\mathbf{S}(\mathbf{R}_2,\mathbf{R}_2,\omega) & \cdots & W_n\mathbf{S}(\mathbf{R}_2,\mathbf{R}_n,\omega)\\ \cdots & \cdots & \cdots & \cdots\\ \cdots & \cdots & \cdots & \cdots\\ W_1\mathbf{S}(\mathbf{R}_n,\mathbf{R}_1,\omega) & W_2\mathbf{S}(\mathbf{R}_n,\mathbf{R}_2,\omega) & \cdots & W_n\mathbf{S}(\mathbf{R}_n,\mathbf{R}_n,\omega) \end{bmatrix}\ . \tag{25}$$

This matrix contains the entire dynamical and structural information on the material system. When the number n remains finite, the self-consistent equation (21) can be solved exactly. It is then possible to obtain the amplitudes of the effective fields $\mathbf{E}(\mathbf{R}_i,\omega)$. Furthermore when the size of the dynamical square matrix $\mathcal{A}(\omega)$ remains reasonable ($n\leq 500$), it is possible to derive accurate numerical solutions for the effective field distribution contained in the supervector $\mathcal{F}(\omega)$.

The discretization procedure described above has a physical meaning if we adopt a microscopic point of view and consider the matter as a set of discrete polarizable entities. In that case, the linear susceptibilities $\chi(\mathbf{R}_k,\omega)$ account for the electromagnetic response of each individual microscopic piece of matter. The density of the discretization grid is then related to the size of the elementary physical components, which can be excited by the incident electromagnetic field $\mathbf{E}_0$. These excitable components scatter the incoming field and their self-consistent interactions build up the electromagnetic near field. This point of view evidences the possible inclusion of quantum susceptibilities, as well as nonlinearities and transient effects in our computational framework. It opens a possible way to study theoretically SNOM imaging of individual molecules adsorbed on surfaces. This is of importance in view of the expected molecular resolution in near-field optics (NFO).[17] This computational scheme can also be extended to the study of localized plasmon resonances occurring near metallic aggregates deposited on flat surfaces. Such calculations need to account for nonlocal effects induced by electrons moving inside the aggregates. As described in Ref. 27, this can be performed by introducing appropriate nonlocal susceptibilities in the self-consistent equation (20).

(ii) Resolution based on the parallel use of Lippmann-Schwinger and Dyson equations.—Instead of solving the Lippmann-Schwinger equation directly, is it also possible to apply an original and robust iterative scheme that allows one to handle accurately very large dynamical matrices.[35,36] This section outlines the main features of this procedure.

Once again, the 3D surface optical system is divided into n discretization meshes. In addition to the discretized Lippmann-Schwinger equation,

$$\mathbf{E}(\mathbf{R}_i,\omega)=\mathbf{E}_0(\mathbf{R}_i,\omega)+\frac{\epsilon(\omega)-1}{4\pi}\sum_{k=1}^{n}W_k\mathbf{S}(\mathbf{R}_i,\mathbf{R}_k,\omega)\cdot\mathbf{E}(\mathbf{r}_k,\omega)\ , \tag{26}$$

we introduce the discretized Dyson's equation

$$\mathcal{S}(\mathbf{R}_i,\mathbf{R}_j,\omega)=\mathbf{S}(\mathbf{R}_i,\mathbf{R}_j,\omega)+\frac{\epsilon(\omega)-1}{4\pi}\sum_{k=1}^{n}W_k\mathbf{S}(\mathbf{R}_i,\mathbf{R}_k,\omega)\cdot\mathcal{S}(\mathbf{R}_k,\mathbf{R}_j,\omega)\ . \tag{27}$$

In Eq. (27), $\mathcal{S}(\mathbf{r},\mathbf{r}',\omega)$ represents the field susceptibility of the entire system. Actually, Dyson's equation (27) is the counterpart of the Lippmann-Schwinger equation for the propagator.[37] In our procedure, we construct the field $\mathbf{E}(\mathbf{R}_i,\omega)$ in the system by solving iteratively Eqs. (26) and (27) in parallel, in the following manner.

At each iteration, we consider an infinitesimal optical system formed by a single mesh of the discretized 3D object. For such a single discretized element, the sum in Eqs. (26) and (27) disappears and these equations can be solved in a straightforward manner to give the field and susceptibility corresponding to a single discretization mesh.[35] To obtain the solution corresponding to the entire system, we start with the incident field $\mathbf{E}_0(\mathbf{R}_i,\omega)$ and the susceptibility $\mathbf{S}(\mathbf{R}_i,\mathbf{R}_k,\omega)$ of the reference system and, by solving Eqs. (26) and (27) rewritten only for this first mesh of the discretized object, we construct the field and the susceptibility corresponding to this infinitesimal surface defect. We then consider the second mesh of the discretized object and, using the results of the preceding step, construct the field and susceptibility corresponding to the 3D object formed by these first two meshes. Proceeding iteratively this way, and considering successively each mesh of the discretized 3D object, we finally obtain the field $\mathbf{E}(\mathbf{R}_i,\omega)$ corresponding to the entire object.

The advantage of this procedure lies in the fact that it replaces the direct solution of the very large system of equations (26) by a succession of small systems of equations, corresponding to each single mesh of the discretized system. This yields an extremely robust numerical scheme, which is able to handle very large physical systems.[35,36]

III. SCATTERING AND LIGHT CONFINEMENT AROUND WELL-CHARACTERIZED SURFACE PROTRUSIONS

Our first example considers a 3D glass defect of parallelepipedic shape lying on a perfectly flat surface (cf. Fig. 3). The optical indexes of both the protrusion and the supporting surface are equal to 1.5. In this application, the reference system is the flat transparent surface, for which the propagator $\mathbf{S}_s(\mathbf{r},\mathbf{r}',\omega)$ is given in the Appendix.[34] Figure 4 displays the behavior of the normalized field intensity defined by

$$I=\frac{|E|^2}{|E_0|^2}\ . \tag{28}$$

In this ratio, E represents the amplitude of the self-consistent field, and E_0 the amplitude of the incident field (i.e., in the absence of the surface defect). The calculation of I is performed in an observation plane parallel to the reference system, placed at a distance Z_0 above the surface. This observation plane is introduced merely for the convenience of data visualization, since the field can be computed for any arbitrary position inside the system by using Eq. (20). The generation of the field above the scatterer was performed with 4900 discretization points. In the internal reflection setup described in Fig. 3, the zeroth-order solution $\mathbf{E}_0(\mathbf{r},\omega)$ is the evanescent field created by total reflection at the surface $Z_0=0$.[9,10,13–17] Such an illumination configuration, introduced in near-field optical microscopy by Ferrell, Reddick, Warmack, and Courjon, Sarayeddine, and Spajer, and Van Hulst and collaborators,[9,10,14] eliminates propagating waves along the z direction. It may be seen in Fig. 4 that the two large-scale (3500×3500) nm^2 calculated images of such mesoscopic objects are rather complex. They display a complicated standing-wave pattern currently observed experimentally in the STOM/PSTM configurations:[28] (1) strong confined field effects just above the scatterer; (2) scattering along its lateral sides

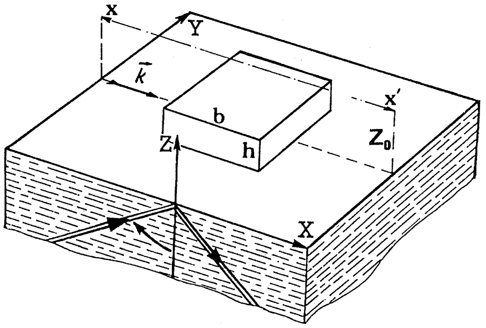

FIG. 3. Perspective drawing of a square-shaped mesoscopic surface defect lying on a flat surface. Protrusion and support have the same optical index (1.5). The system is illuminated in total reflection and the incident wavelength in vacuum is equal to 620 nm. The object height is $h=100$ nm and the side of its square section $b=550$ nm; $\mathbf{k}$ represents the surface wave vector associated with the excitation field.

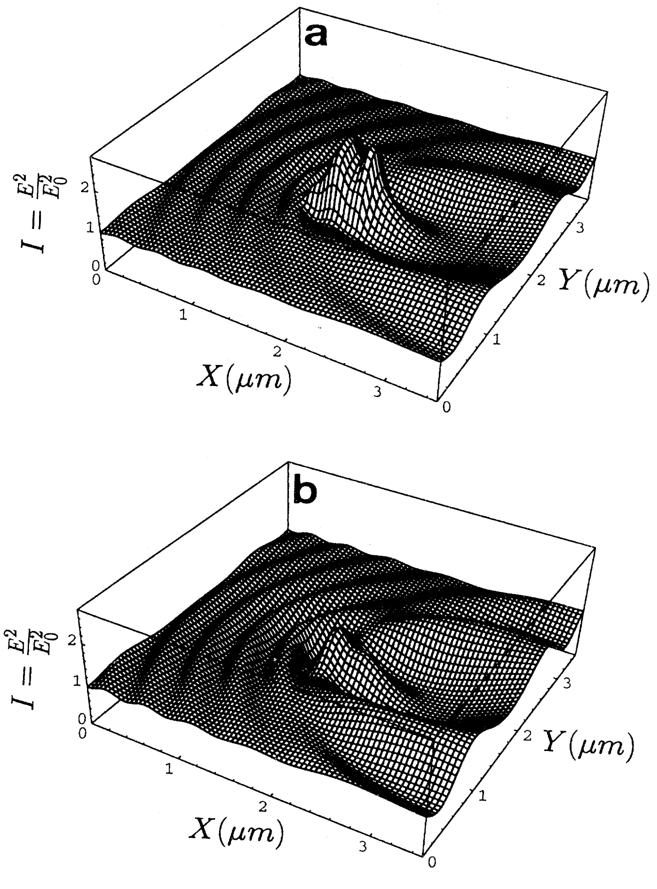

FIG. 4. 3D perspective view of the normalized electric field intensity $I(X,Y)=|E|^2/|E_0|^2$, calculated above the scattering system schematized in Fig. 3. The calculation is performed in the TM polarization mode. For the convenience of the data visualization, the numerical data $I(X,Y)$ have been calculated in an observation plane located at a distance Z_0 above the flat surface: (a) $Z_0=150$ nm; (b) $Z_0=200$ nm.

and classical interference patterns due to the interaction between the traveling surface wave and the surface wave reflected by the defect. In particular, Fig. 4 indicates that about 50 nm above the top of the object, the enhancement factor of the field intensity reaches 2.5. In contrast with the fringe pattern, which reveals pure propagation phenomena, the amplitude and the extension of the light confinement observed above the object dramatically depend on the approach distance Z_0. Indeed, one observes in Fig. 4(b) a drastic reduction of the light intensity above the protrusion, where Z_0 increases by 50 nm. We have further investigated this aspect and give in Fig. 5 two cross sections corresponding to Figs. 4(a) and 4(b), respectively. Two different phenomena are highlighted by Fig. 5. First, as already mentioned, increasing the observation height leads to a weakening of the light confinement effect. Such behavior is consistent with the short-range decaying of optical near-field effects. Second, the modification of the observation distance introduces a significant distortion in the intensity profile itself. Typically, one observes a strong reduction of the field intensity above the right edge of the square-shaped protrusion when increasing Z_0. Actually, the amplitude of this distortion effect critically depends on the ratio

$$\eta = bk/2\pi \ , \tag{29}$$

between the lateral extension b of the object and the surface wavelength $2\pi/k$. This phenomenon could explain the lost resolution often observed in the vicinity of certain mesoscopic surface structure edges. A shift in the standing wave is also observed between the two observation distances. Furthermore, as described in the recent experimental works of Van Hulst, Segering, and Bolger,[28] generally for larger objects the interference phenomenon dominates and makes the detection of subwavelength features difficult.

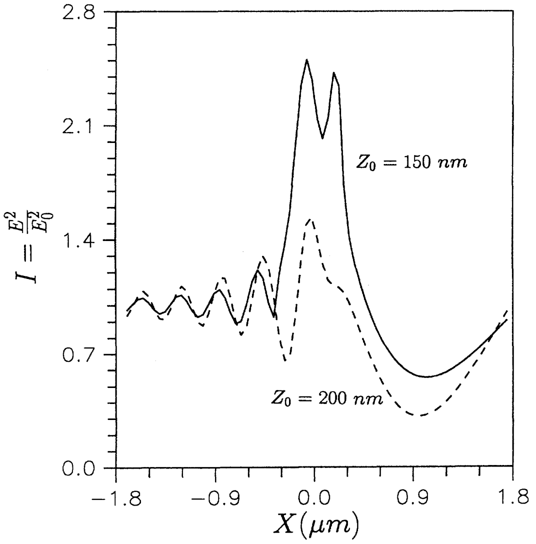

FIG. 5. Variation of the normalized electric field intensity along the xx' straight line defined in Fig. 3. These cross sections, issued from the 3D maps of Fig. 4, have been calculated for the same approach distances Z_0.

So far, we have proved with this introductory simulation that, first, the 3D objects confine the electromagnetic field around them and, second, that the relation between the object profile and the resulting spatial field distribution may be very complex. Actually, this result forces us to address a fundamental question in NFO: what would be both optimal lighting configuration and optimal object dimension for which the field distribution would tend to perfectly reproduce the object profile? In order to answer this important question we consider a second application with a more complex system composed of seven identical square-shaped pads (cf. Fig. 6). The dielectric parameters are the same as those used in the previous application. We present in Fig. 7 a first simulation by illuminating this system in TM polarization. Each dielectric pad is 100 nm high and has a section of $(0.25 \times 0.25)\ \mu m^2$ and the calculation is performed in the plane $Z_0 = 120$ nm. In order to emphasize both interference and scattering effects occurring around the obstacles, we have used a large computational window $7 \times 7\ \mu m^2$. Due to the large spacing between each individual scatterer (1.75 μm), the resulting field pattern is a complex mixture of interference phenomena due to multiple reflections between the different pads. As expected, when the number of defects per unit area increases, the standing-wave pattern arising from the multiple-scattering effects gives rise to the well-known "speckle pattern" phenomenon.

In order to gain more insight into the relation between the field pattern and object profile relation, we study in Fig. 8 the evolution of the image upon reduction of the different geometrical parameters P_1, P_2, and H defined in Fig. 6. The two commonly used polarization modes TE and TM are simultaneously considered in Figs. 8(a), 8(b), and 8(c). Three different typical sizes are successively investigated. In the first example [Fig. 8(a)] we start in the mesoscopic range ($P_1 = 250$ nm, $P_2 = 1750$ nm, and $H = 100$ nm). In the two other examples [Figs. 8(b) and 8(c)], a reduction factor equal to 2 and 4 is applied, and

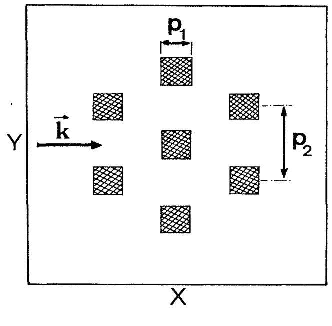

FIG. 6. Top view of a 3D object composed by seven identical square-shaped protrusions. The dielectric parameters are the same as those used in the previous application. The center of each pad is located at the nodes of a hexagonal pattern of side P_2. P_1 represents the dimension of each individual protrusion. The system is illuminated in internal reflection configuration and $\mathbf{k}$ represents the surface wave vector. For the same incident wavelength, three different object sizes, defined by the parameters P_1 and P_2, will be successively investigated in Figs. 8(a), 8(b), and 8(c), respectively. The height of the pads is H.

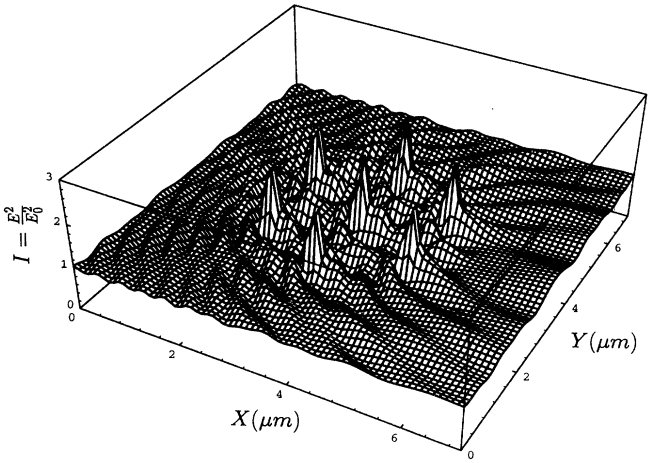

FIG. 7. 3D perspective view of the normalized electric field intensity $I(X,Y)=|E|^2/|E_0|^2$ calculated above the scattering system schematized in Fig. 6. The observation plane is located at a distance $Z_0=120$ nm above the flat surface. This large-scale calculation (7×7) μm^2 has been performed in the TM mode. The parameters P_1 and P_2 are equal to 250 and 1750 nm, respectively and the pads are 100 nm high.

the position of the observation plane is reduced in the same proportion.

The evolution of the field pattern raises the following comments: (i) First, when the object displays mesoscopic dimensions [see Figs. 7 and 8(a)], the distribution is dominated by interference phenomena, so that the field lines do not follow the profile of the square-shaped protrusions. (ii) Second, as the dimensions of the 3D objects enter the subwavelength range [cf. Figs. 8(b) and 8(c)], the interference pattern around the objects progressively collapses and the field distribution tends to become perfectly symmetrical, thereby reproducing the symmetry of the pads. Under such conditions, and in TE polarization, a highly localized field occurs just above the edges located in a perpendicular direction to the incident field E_0. In fact, when we deal with such subwavelength-sized objects, the importance of retardation effects decreases dramatically, so that the symmetry of the field distribution is only governed by both the orientation of the incident field and the profile of the object itself. Actually, these features may help us to get more insight into the complex contrast phenomenon observed in the TE mode. The field distribution is now governed by the depolarization effects that result from the conservation of the normal component of the displacement vector $\mathbf{D}(\omega)=\epsilon(\omega)\mathbf{E}(\omega)$ when crossing the surfaces of the dielectric protrusions. Due to the rapid variation of the dielectric constant between air and glass, this conservation imposes a sharp variation of the field near the interfaces perpendicular to E_0.

A completely different behavior is observed with the TM mode. In this polarization the surface wave is mainly dominated by the Z component of the incident field. The main resulting effect is, as expected, a better image-object relation in the subwavelength range. One can observe that, when the size of the square-shaped protrusions is gradually reduced, the field distribution around the objects tends to perfectly reproduce their profiles.

IV. CONCLUSION

We have reported theoretical results on the scattering between electromagnetic surface waves and well-characterized localized surface defects. By discretizing the entire space occupied by the protrusions we have derived the exact solution of the complete field distribution resulting from the light-matter interaction. This technique has proven to be extremely powerful and versatile for studying experimental situations currently encountered in SNOM. Furthermore, this method can easily be extended to handle anisotropic materials, which is extremely important for the application of NFO to magneto-optical data storage, as well as for the understanding of the near-field optical interaction with molecular systems that display anisotropical response properties. In the different simulations presented in this paper the surface protrusions are excited by a monochromatic surface wave generated by total reflection. A striking difference of behavior was found, depending on both the obstacle size and the polarization state of the traveling wave along the surface. In the subwavelength range, the TM polarization mode allows one to reproduce the shape of the objects, whereas a TE polarized wave can be used to extract information on the contours of the objects themselves. Finally, the most remarkable feature is the considerable reduction of the importance of collective effects between surface structures when we gradually enter the subwavelength regime.

ACKNOWLEDGMENTS

This work was performed in the framework of the Human Capital and Mobility Program "Near-field Optics for Nanoscale Science and Technology" initiated by the European Community and with a grant of the CNRS-ULTIMATECH Program (France).

APPENDIX: THE RETARDED FIELD SUSCEPTIBILITY $\mathbf{S}_s$ OF A PLANE DIELECTRIC INTERFACE

In the particular case of a solid limited by a perfectly planar surface, various theoretical methods have been developed to derive this dyadic tensor.[29–34] In this Appendix, we use a similar procedure to that described by Agarwal,[30] to derive the retarded field susceptibility associated with a plane dielectric interface. First, we start from the standard dipolar source field expression:

$$\mathbf{E}_m(\mathbf{r},\omega)=\mathbf{S}_0(\mathbf{r},\mathbf{r}_0,\omega)\cdot\mathbf{m}(\omega)\ , \tag{A1}$$

where $\mathbf{m}(\omega)$ represents an arbitrary fluctuating dipole moment located at $\mathbf{r}_0$ and $\mathbf{S}_0(\mathbf{r},\mathbf{r}_0,\omega)$ is the free-space dyadic propagator derived in Sec. II A, Eq. (13). Because of the specific symmetry of a bare plane interface, it is useful to expand the free-space scalar Green's function $\mathcal{G}_0(\mathbf{r},\mathbf{r}',\omega)$ contained in $\mathbf{S}_0(\mathbf{r},\mathbf{r}_0,\omega)$ into a Weyl series:[30]

$$\mathcal{G}_0(\mathbf{r},\mathbf{r}',\omega)=\frac{i}{2\pi}\int\int\frac{d\mathbf{k}}{w_0}\exp[i\mathbf{k}\cdot(\mathbf{l}-\mathbf{l}')+iw_0|z-z'|]\,, \tag{A2}$$

with $\mathbf{r}=(\mathbf{l},z)$, $\mathbf{r}'=(\mathbf{l}',z')$, $\mathbf{k}=(k_x,k_y)$, and $w_0^2=\frac{\omega^2}{c^2}-k^2$ [with $\mathrm{Im}(w_0)\geq 0$]. Introducing this relation into Eq. (13), one finds

$$\mathbf{S}_0(\mathbf{r},\mathbf{r}',\omega)=\frac{i}{2\pi}\int\int\frac{d\mathbf{k}}{w_0}\left[\mathbf{I}\frac{\omega^2}{c^2}+\mathcal{K}\mathcal{K}]\exp[i\mathbf{k}\cdot(\mathbf{l}-\mathbf{l}')+iw_0|z-z'|\right]\,, \tag{A3}$$

with $\mathcal{K}=[\mathbf{k},w_0\mathrm{sgn}(z-z')]$. The source field above the surface is then given by

$$\mathbf{E}_m(\mathbf{r},\omega)=\frac{i}{2\pi}\int\int\frac{d\mathbf{k}}{w_0}\left[\mathbf{I}\frac{\omega^2}{c^2}+\mathcal{K}\mathcal{K}]\exp[i\mathbf{k}\cdot(\mathbf{l}-\mathbf{l}_0)+iw_0|z-z_0|\right]\cdot\mathbf{m}(\omega)\,. \tag{A4}$$

The presence of the source field $\mathbf{E}_m(\mathbf{r},\omega)$ modifies the local field above the surface. In fact, the solid generates an additional contribution, the so-called response field $\mathbf{E}_r(\mathbf{r},\omega)$ that must be added to $\mathbf{E}_m(\mathbf{r},\omega)$ itself. The determination of this response field includes the following well-known steps:[30] expansion of $\mathbf{E}_r(\mathbf{r},\omega)$ in plane waves and application of the standard electromagnetic boundary conditions at the surface $z=0$. This procedure leads

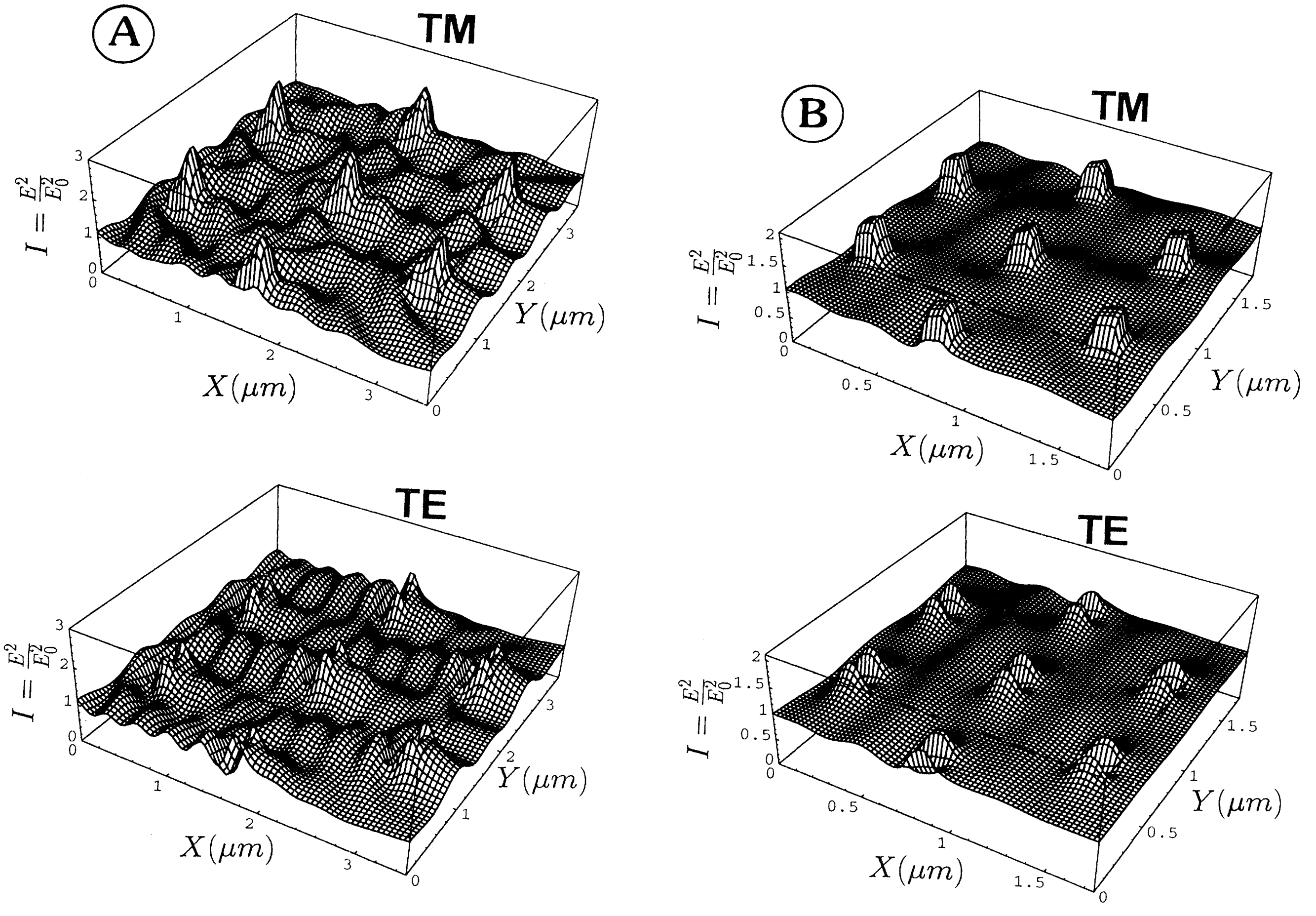

FIG. 8. A sequence of 3D maps $I(X,Y)=|E|^2/|E_0|^2$ describing the evolution of the standing field pattern observed around the topographic object described in Fig. 6. For the same incident wavelength $\lambda=620$ nm, the volume occupied by this object is progressively reduced. (a) We start in the mesoscopic range with $P_1=250$ nm, $P_2=1750$ nm, and $Z_0=120$ nm. The height H of each pad is 100 nm, the computational window (3.5×3.5) μm^2 is centered around the structure, and the two usual polarization modes have been treated. (b) Same calculation, but after reduction of all the lengths by a factor 2: $P_1=125$ nm, $P_2=875$ nm, $Z_0=60$ nm, and the height H of each pad is 50 nm. (c) The reduction factor now reaches 4: $P_1=67.5$ nm, $P_2=437.5$ nm, $Z_0=30$ nm, and the height H of each pad is 25 nm.

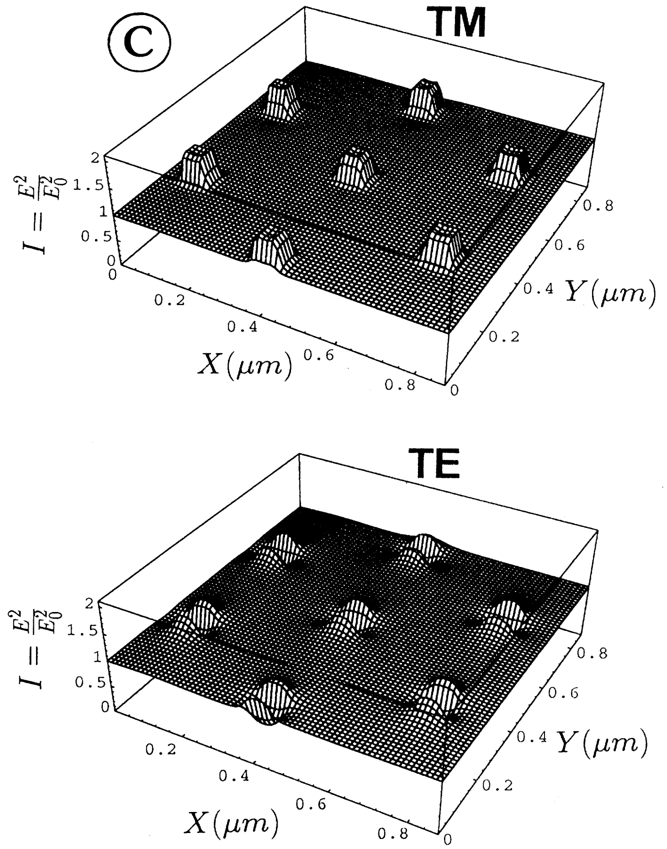

FIG. 8. (*Continued*).

to a linear relation between the response field and the magnitude of the dipole $\mathbf{m}(\omega)$ itself

$$\mathbf{E}_r(\mathbf{r},\omega)=\mathbf{S}_s(\mathbf{r},\mathbf{r}_0,\omega)\cdot\mathbf{m}(\omega)\ , \tag{A5}$$

where the dyadic $\mathbf{S}_s(\mathbf{r},\mathbf{r}_0,\omega)$ is defined by

$$\mathbf{S}_s(\mathbf{r},\mathbf{r}_0,\omega)=\frac{i}{2\pi}\int\int d\mathbf{k}\mathcal{F}(\mathbf{r},\mathbf{r}_0,\omega)\mathbf{N}(\mathbf{k},\omega)\ . \tag{A6}$$

The quantity $\mathcal{F}(\mathbf{r},\mathbf{r}_0,\omega)$ is a scalar spatial function that connects two points $\mathbf{r}$ and $\mathbf{r}'$ above the surface,

$$\mathcal{F}(\mathbf{r},\mathbf{r}_0,\omega)=\exp[i\mathbf{k}\cdot(\mathbf{l}-\mathbf{l}_0)+iw_0(z+z_0)]\ , \tag{A7}$$

and $\mathbf{N}(\mathbf{k},\omega)$ is a second rank tensor that contains the optical response properties of the solid

$$\mathbf{N}((\mathbf{k},\omega))=\begin{bmatrix} \Delta_p w_0\frac{k_x^2}{k^2}-\Delta_s\frac{\omega^2k_y^2}{c^2w_0k^2} & \Delta_p w_0\frac{k_xk_y}{k^2}+\Delta_s\frac{\omega^2k_xk_y}{c^2w_0k^2} & \Delta_p k_x \\ \Delta_p w_0\frac{k_xk_y}{k^2}+\Delta_s\frac{\omega^2k_xk_y}{c^2w_0k^2} & \Delta_p w_0\frac{k_y^2}{k^2}-\Delta_s\frac{\omega^2k_x^2}{c^2w_0k^2} & \Delta_p k_y \\ -\Delta_p k_x & -\Delta_p k_y & -\Delta_p\frac{k^2}{w_0} \end{bmatrix}\ . \tag{A8}$$

In this equation, the two reflection coefficients Δ_p and Δ_s are both functions of the optical dielectric constant $\epsilon_s(\omega)$ of the solid:

$$\Delta_p=\frac{w-\epsilon_s(\omega)w_0}{w+\epsilon_s(\omega)w_0}\quad\text{and}\quad\Delta_s=\frac{w-w_0}{w+w_0}\ , \tag{A9}$$

with

$$w=\left[\epsilon_s\frac{\omega^2}{c^2}-k^2\right]^{1/2}\ . \tag{A10}$$

When the dimensions of the physical system under study are small, $\mathbf{S}_s(\mathbf{r},\mathbf{r}_0,\omega)$ reduces to the well-known electrostatic form:[29]

$$\mathbf{S}_s(\mathbf{r},\mathbf{r}',\omega)=\frac{1}{2\pi}\frac{\epsilon_s(\omega)-1}{\epsilon_s(\omega)+1}\int\frac{d\mathbf{k}}{k}e^{i\mathbf{k}\cdot(\mathbf{l}-\mathbf{l}_0)-k(z+z_0)}\begin{bmatrix} k_x^2 & k_xk_y & ikk_x \\ k_xk_y & k_y^2 & ikk_y \\ -ikk_x & -ikk_y & k^2 \end{bmatrix} . \tag{A11}$$

---

[1] E. H. Singe, Philos. Mag. **6**, 356 (1928).

[2] H. A. Bethe, Phys. Rev. **66**, 163 (1944).

[3] E. A. Ash and G. Nichols, Nature **237**, 510 (1972).

[4] U. Ch. Fischer and H. P. Zingsheim, J. Vac. Sci. Technol. **19**, 881 (1981).

[5] D. W. Pohl, W. Denk, and M. Lanz, Appl. Phys. Lett. **44**, 651 (1984).

[6] A. Lewis, M. Isaacson, A. Harootunian, and A. Muray, Ultramicroscopy **13**, 227 (1984).

[7] U. Ch. Fischer, J. Vac. Sci. Technol. B **3**, 386 (1985).

[8] A. Harootunian, E. Betzig, M. Isaacson, and A. Lewis, Appl. Phys. Lett. **49**, 674 (1986).

[9] R. Reddick, R. J. Warmack, and T. J. Ferrell, Phys. Rev. B **39**, 767 (1989).

[10] D. Courjon, K. Sarayeddine, and M. Spajer, Opt. Commun. **71**, 23 (1989).

[11] E. Betzig, J. K. Trautman, T. D. Harris, J. S. Weiner, and R. L. Kostelak, Science **251**, 1468 (1991), and references therein.

[12] K. Lieberman and A. Lewis, Ultramicroscopy **42-44**, 399 (1991).

[13] T. L. Ferrell, S. L. Sharp, and R. J. Warmack, Ultramicroscopy **42-44**, 408 (1991).

[14] N. F. Van Hulst, F. B. Segerink, F. Achten, and B. Bolger, Ultramicroscopy **42-44**, 416 (1992).

[15] F. de Fornel, L. Salomon, P. Adam, E. Bourillot, J. P. Goudonnet, and M. Nevière, Ultramicroscopy **42-44**, 422 (1992).

[16] M. Specht, J. D. Pedarnig, W. M. Heckl, and T. W. Hansch, Phys. Rev. Lett. **68**, 476 (1992).

[17] E. Betzig and R. J. Chichester, Science **262**, 1422 (1993).

[18] For a historical presentation of near-field optics, see for example, D. W. Pohl, in *Near Field Optics*, Vol. 242 of *NATO Advanced Study Institute, Series E: Applied Sciences*, edited by D.W. Pohl and D. Courjon (Kluwer, Dordrecht, 1993), pp. 1–5.

[19] D. Courjon, C. Bainier, and F. Baida, Opt. Commun. **110**, 7 (1994).

[20] P. Dawson, F. de Fornel, and J. P. Goudonnet, Phys. Rev. Lett. **72**, 2927 (1994).

[21] M. Chudgar, A. Choo, H. Jackson, G. De Brabander, M. Kumar, and J. Boyd, Ultramicroscopy (to be published).

[22] C. Girard and D. Courjon, Phys. Rev. B **42**, 9340 (1990).

[23] A. Dereux, Ph.D. thesis, Faculté Universitaire N. D. de la Paix, Namur, Belgium, 1991.

[24] A. Dereux, J. P. Vigneron, Ph. Lambin, and A. A. Lucas, Physica (Amsterdam) B **175**, 65 (1991).

[25] A. A. Lucas, J. P. Vigneron, Ph. Lambin, Th. Laloyaux, and I. Derycke, Surf. Sci. **269**, 74 (1992).

[26] C. Girard, A. Dereux, and O. J. F. Martin, Phys. Rev. B **49**, 13 872 (1994).

[27] C. Girard and A. Dereux, Phys. Rev. B **49**, 11 344 (1994).

[28] N. F. Van Hulst, F. B. Segering, and B. Bolger, Opt. Commun. **87**, 212 (1992).

[29] A. D. McLachlan, Mol. Phys. **7**, 381 (1964).

[30] G. S. Agarwal, Phys. Rev. A **11**, 230 (1975).

[31] H. Metiu, J. Chem. Phys. **76**, 1765 (1982).

[32] H. Metiu, Prog. Surf. Sci. **17**, 153 (1984).

[33] H. Metiu and P. Das, Annu. Rev. Phys. Chem. **35**, 507 (1984).

[34] C. Girard and X. Bouju, J. Chem. Phys. **95**, 2056 (1991).

[35] O. J. F. Martin, A. Dereux, and C. Girard, J. Opt. Soc. Am. A **11**, 1073 (1994).

[36] O. J. F. Martin, Ph.D. thesis, EPFL Lausanne, Switzerland, 1993.

[37] E. N. Economou, *Green's Functions in Quantum Physics*, 2nd ed. (Springer-Verlag, Berlin, 1990).